

Three-dimensional reconstruction of statistically optimal unit cells of polydisperse particulate composites from microtomography

H. Lee,¹ M. Brandyberry,¹ A. Tudor,¹ and K. Matouš^{2,*}

¹Computational Science and Engineering, University of Illinois at Urbana–Champaign, Urbana, Illinois 61801, USA

²Department of Aerospace and Mechanical Engineering, University of Notre Dame, Notre Dame, Indiana 46556, USA

(Received 19 August 2009; published 9 December 2009)

In this paper, we present a systematic approach for characterization and reconstruction of statistically optimal representative unit cells of polydisperse particulate composites. Microtomography is used to gather rich three-dimensional data of a packed glass bead system. First-, second-, and third-order probability functions are used to characterize the morphology of the material, and the parallel augmented simulated annealing algorithm is employed for reconstruction of the statistically equivalent medium. Both the fully resolved probability spectrum and the geometrically exact particle shapes are considered in this study, rendering the optimization problem multidimensional with a highly complex objective function. A ten-phase particulate composite composed of packed glass beads in a cylindrical specimen is investigated, and a unit cell is reconstructed on massively parallel computers. Further, rigorous error analysis of the statistical descriptors (probability functions) is presented and a detailed comparison between statistics of the voxel-derived pack and the representative cell is made.

DOI: [10.1103/PhysRevE.80.061301](https://doi.org/10.1103/PhysRevE.80.061301)

PACS number(s): 45.70.-n, 05.20.-y, 46.65.+g, 87.59.-e

I. INTRODUCTION

Computational methods based on particulate packs are commonly used in variety of scientific disciplines. For example, particulate packs have been used in modeling of heterogeneous materials, such as solid propellants [1,2], granular media [3], protein folding [4], and low-temperature phases of matter such as liquids, crystals, and glasses [5]. Moreover, packing problems are common in information theory [6] and many different branches of pure mathematics [7]. A study of these systems in a computational framework usually starts with a model of the morphology, such as a packing algorithm. Therefore, a packing algorithm to guide these models has been in the forefront of mathematical and scientific investigations for many decades, and this fascination led to development of several packing codes that are capable of producing high-quality polydisperse heterogeneous packs [8–10].

Recently, new developments in three-dimensional (3D) imaging using microtomography (micro-CT) have also ushered in the rapid expansion of statistical modeling techniques that investigate the morphology and the microstructure characterization of widely used material systems, such as propellants [11,12], glass beads [13], paper [14], and engineered cementitious composites [15], just to name a few. An example of the complicated microstructures obtained from the micro-CT can be seen in Fig. 1.

The subsequent statistical characterization is usually performed, for both computationally and/or tomographically obtained packs, in order to understand the internal structure of these systems. The need for such understanding and importance of the higher-order statistics start with early work of Bernal [16] who investigated the geometrical structure of liquids using the radial distribution function. Significance of

statistical description galvanized several research communities in condensed matter physics and far beyond, with applications in non-Gaussian noise as a tool to study disordered materials [17], and application of Minkowski functionals in analysis of background cosmic radiation [18], just to name a few. Moreover, the analysis of higher-order statistics, in the guise of the analysis of x-ray speckle, is increasingly gaining attention among condensed matter physicists [19].

Unfortunately, both computationally and/or tomographically derived packs are often too large to be uniformly resolved in practical numerical simulations of combustion phenomena [1], nonlinear viscoelastic response of a binder [20], or damage evolution along the particle-matrix interface [21]. Therefore, many researchers have devoted their attention to finding a statistically optimal unit cell. Povirk [22] proposed a method for determining periodic microstructures in two dimensions that are statistically similar to more complex, random, two-phase microstructures by using a certain statistical descriptor function. Yeong and Torquato [23,24] proposed a method for the reconstruction of random media based on two-point probability functions using simulated annealing (SA) and two-dimensional material slices. Bochenek and Pyrz [25] also used the simulated annealing procedure in conjunction with a pair correlation function and a stress interaction parameter to reconstruct a unit cell in three dimensions. However, the simple pair correlation function used in their work did not represent the disparate particle modes, and thus, the probability spectrum optimized in [25] was restricted. Zeman and Šejnoha [26] examined three considerably different material systems, a fiber composite, a woven composite, and a masonry, to demonstrate the reconstruction using two-point probability functions and the lineal path function, yet again, only two-dimensional images of microstructures have been employed.

Recently, Jiao *et al.* [27,28] reconstructed a three-dimensional realization of Fontainebleau sandstone and a boron-carbide or aluminum composite from two-dimensional

*Corresponding author; kmatous@nd.edu

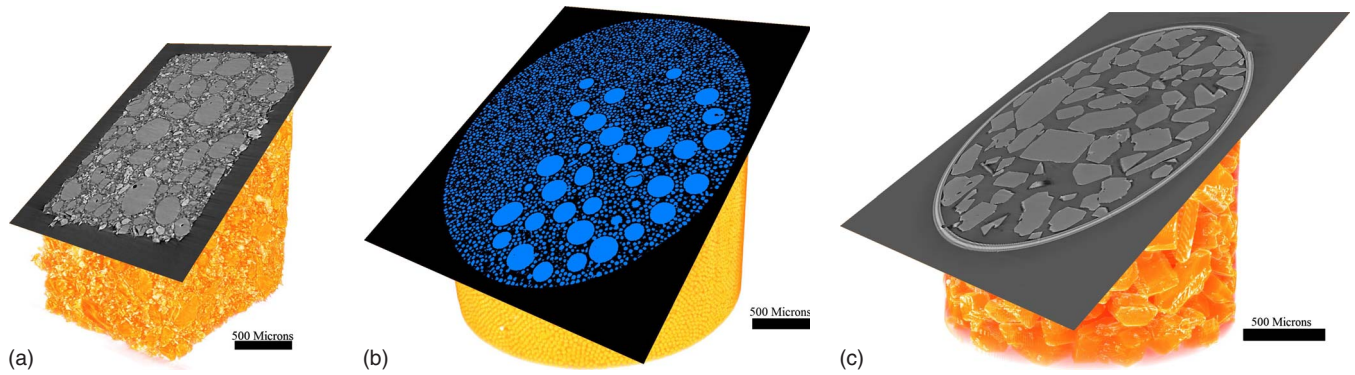


FIG. 1. (Color online) Typical members of the micro-CT based ensemble. (a) Heterogeneous propellant. (b) Glass beads system. (c) Table sugar.

tomographic images using second-order statistics and a “lattice-point” algorithm. In their work, a lattice or a voxel-based reconstruction is used for a two-phase medium in conjunction with a basis function approximation of the correlation functions for a faster probability function evaluation. Fullwood *et al.* [29] also used a voxel-based phase-recovery algorithm for reconstruction of three-dimensional polycrystals. Their method is based on a fast discrete Fourier transform, and thus, its parallelization is cumbersome and the domain analyzed in the paper is relatively small, as pointed out later. Although relatively simple, the pixel or voxel-based representation of microstructure simplifies the geometrical considerations since any geometrical object, such as a sphere, a rhombus, etc., is approximated by a cluster of voxels, and thus, the resolution is highly pixel or voxel dependent. Moreover, for many physical phenomena, such as a particle decohesion, the voxel-based representation is inappropriate due to the steplike interface representation.

Similar to our approach described hereafter is the work of Seidler *et al.* [30]. In their paper, granules are first mapped to spheres, as in our work, and several statistical measures, such as cylindrical density, radial distribution function, and bond orientational correlation function, are computed. However, only limited micro-CT data of an almost ideally monodisperse system (glass spheres with $d=63 \mu\text{m}$ and $>95\%$ having polydispersivity of $\pm 4 \mu\text{m}$) were used in their work with only 2000 granules in the system and only 359 granules used for statistics evaluation. In our work, we scan 19 892 polydisperse particles and statistically characterize 19 123 of them. We also show that a statistically optimal and thus the smallest possible unit cell consists of 1082 spheres. Therefore, it is unlikely that 359 inclusions can be used for detailed morphology characterization even though the monodisperse system likely requires fewer particles in the cell compared to our polydisperse one. Moreover, the selected statistical descriptors in [30] are limited to spherical geometries, whereas our concept based on n -order probability functions is general and easily applicable to general non-spherical shapes, such as crystals.

Different from the sampling based methods described above is the analysis based on Minkowski functionals [31,32]. In three dimensions the functionals are related to the familiar measures of volume fraction, surface area, integral mean curvature, and Euler characteristic, such as connectiv-

ity of pores. The heterogeneous material is represented by a Boolean model, where *overlapping grains* of various shape and sizes are used to reconstruct a material morphology. Although mathematically elegant, Minkowski functionals are better suited for two-phase porous media, such as soils or sedimentary rocks, due to the overlapping nature of the algorithm, and this elegance would be lost if a constraint on the particle interpenetration were to be introduced.

Another approach introduced by Sundararaghavan and Zabaras [33] employs support vector machines for three-dimensional reconstruction of microstructures using limited statistical information available from planar images. Quintanilla and Max Jones used convex quadratic programming to model random media with Gaussian random fields [34].

In this work, we reconstruct a fully three-dimensional polydisperse medium, such as a heterogeneous solid propellant [Fig. 1(a)], from three-dimensional tomographic data. We make no assumptions about the probability functions and discretize them numerically with high detail. The full probability spectrum, not just a single function, and the geometrically exact shape of particles, not just a voxel simplification, are used in our approach, yielding a multidimensional optimization problem with a highly complex objective function. Therefore, we perform the reconstruction on massively parallel computers. The present paper is an extension on our earlier work [35,36], where two-dimensional periodic cells of trimodal fibrous composites and three-dimensional trimodal particulate composites were reconstructed, emphasizing the discrete nature of the entire probability spectrum and the proper geometrical particle shape representation. Here, we advance this methodology to the reconstruction of polydisperse particulate systems from rich three-dimensional tomographic data. Moreover, we compute the third-order probability functions, comment on their basic features, and compare their characteristics for the tomographic data and our statistically equivalent cells. (Analysis of higher-order statistics was often omitted in the papers mentioned above.) Our codes, STAT3D and RECON3D, compute the statistics and reconstruct a representative unit cell (RUC) in parallel using message passing interface, allowing for large domains to be efficiently evaluated ($\sim 66 \times 10^6$ voxels), higher statistical moments to be computed accurately, and the optimal computational domains to be generated quickly. Their parallel linear scalability has been shown in [36].

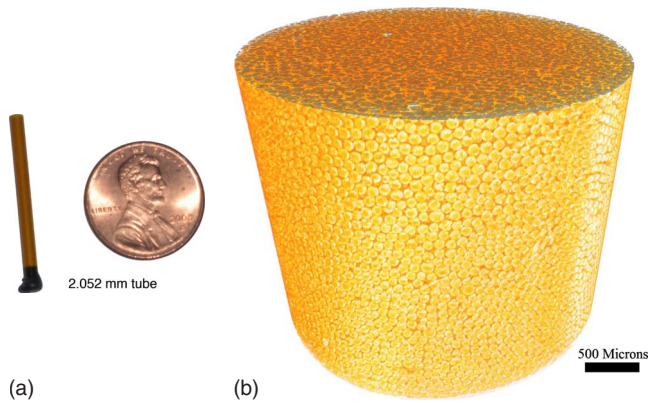


FIG. 2. (Color online) (a) Plastic tube used in scanning experiments. (b) Polydisperse glass bead system.

The remainder of the paper is organized as follows. In Sec. II, we discuss the sample preparation, the tomographic imaging, and the image processing. For clarity of presentation, Sec. III describes the basic concepts of the probability functions and details the morphology of the glass bead system to mimic a complex heterogeneous solid propellant [Fig. 1(a)]. In Sec. IV, we comment on the reconstruction procedure and compare the statistically representative unit cell and its statistics to the original tomographically observed medium with the statistical functions described in Sec. III. Finally, some conclusions are drawn in Sec. V.

II. SAMPLE PREPARATION, MICRO-CT SCANNING, AND IMAGE PROCESSING

We prepare a sample pack of spherical glass beads with average diameter of $44 \mu\text{m}$ in a 2.052 mm diameter scanning tube with one end blocked with epoxy (Fig. 2). The glass beads were manufactured by Crystal Mark, Inc., and 98% of the beads by weight are of diameters between 35 and $58 \mu\text{m}$. In order to prepare as uniform sample as possible, the beads were filtered in two steps. First, to remove hollow particles, the beads were submerged in a water bath and stirred. The hollow beads floating on the water surface were removed and the remaining ones were completely dried. Second, the nonspherical particles were removed by rolling them

down on an inclined plane and removing beads that would not roll. After this preparation, we poured the filtered beads slowly into the tilted tube where a piece of thread was placed in the middle of the container before pouring. The thread was pulled out slowly. A similar method to randomize a pack by pulling a stick out was previously used by Aste *et al.* [13]. The tube was tapped on the side, the bottom and the top. The beads were slightly compressed from above during the tapping procedure.

The final sample is scanned by an Xradia micro-CT machine. The resulting resolution for this scan is $2.818 \mu\text{m}$ per voxel. The three-dimensional image reconstruction is shown in Fig. 2(b). The 64-bit quantification pack for AMIRA 5.2 is used to gather the information specific to each particle, i.e., the position of the particle center and the individual particle volume. To characterize this random medium, we first acquire a block ($1445.372 \times 1287.892 \times 789.106 \mu\text{m}^3$) from the core of the 3D scanned image in Fig. 2. This represents $513 \times 457 \times 280 = 65\,643\,680$ voxels, which is 29.89 times higher resolution to that used by Fullwood *et al.* [29], where only $130 \times 130 \times 130 = 2\,197\,000$ voxels were analyzed.

The particles in contact are identified and separated through the separation procedure in AMIRA. This leads to a small volume removal. In the present case, the packing fractions from the original voxel pack are 0.574 before the separation and 0.553 after the separation, and thus we have 2.1% loss of the packing volume due to the separation. It is known that the packing fraction for a stable conglomeration of polydisperse spheres ranges from 0.55 to 0.64 and even up to 0.74 in the crystalline state [37]. Considering the role of the interparticle forces such as friction [38,39], the packing fraction of our pack is well ranged. In Fig. 3(b), most of the particles are now clearly separated from each other. At the final stage of the process 19 892 particles are identified in the region of observation.

Despite the physical filtering to remove extra small or hollow particles, we observe debris of very small sizes forming a peak around $4 \mu\text{m}$ diameter in Fig. 3(a). However, the volume fraction of these particles is very small and can be neglected. Here we remove the beads with diameters less than $7 \mu\text{m}$. The remaining particles are separated into nine discrete bins as depicted in Fig. 3(a). Next, a pack based on the sizes and the locations of the individual beads is gener-

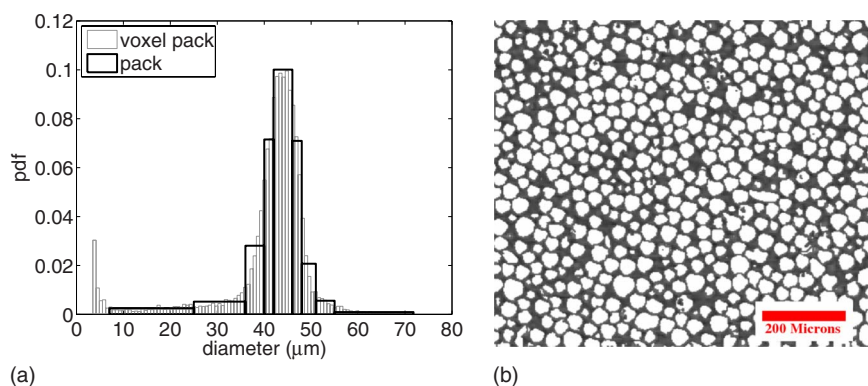


FIG. 3. (Color online) (a) Probability density function and a new binning of the particle sizes. Nine discrete bins are used to capture the original distribution. Note the debris for $d < 7 \mu\text{m}$. (b) Two-dimensional slice through the voxel pack. Particle separation is done in AMIRA.

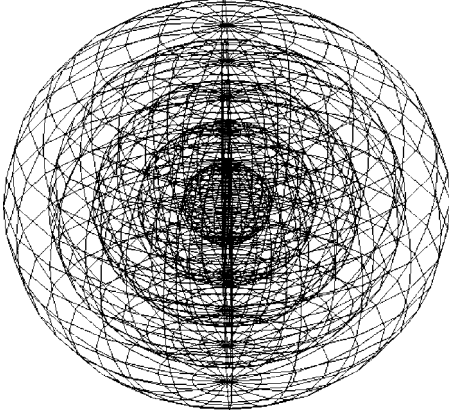


FIG. 4. Three-dimensional sampling template with 5 radial points and 20 circumferential points for illustration.

ated and used to obtain the statistical properties of the actual material. In generating the pack, we replace all the beads with spheres, which causes 0.05% overall particle overlap. The overlap is calculated as $V_o/V_p \times 100$, where V_o is the volume of overlap between particles and V_p is the total volume of the particles. The final pack has 19 123 spherical particles. We note that the tomographic pack after the image processing is called the “voxel pack” and the pack generated based on the voxel data by replacing the inclusions with spheres is called the “pack” hereafter.

III. STATISTICAL MORPHOLOGY OF COMPOSITES

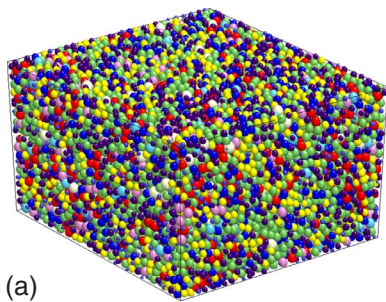
It is generally accepted that the effective properties of a heterogeneous material do not depend only on the properties of each phase but also on the interactions between the material phases. In a statistical sense, both the volume fraction of each phase and various correlation functions between the phases are fundamental in determining the material properties [40,41]. In this section, we discuss one-, two-, and three-point probability functions to characterize the morphology of a heterogeneous medium [41,42].

A. Probability functions

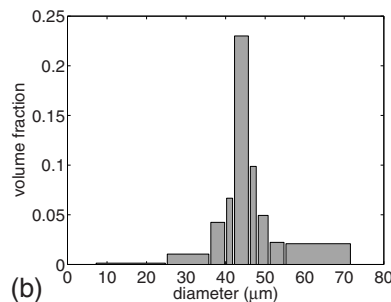
To describe the probability functions, we consider a phase indicator function at a position \mathbf{x} in a sample α of an ensemble space \mathcal{E} ,

$$\chi_r(\mathbf{x}; \alpha) = \begin{cases} 1 & \text{if } \mathbf{x} \text{ in phase } r \\ 0 & \text{otherwise.} \end{cases} \quad (1)$$

The ensemble average is given by



(a)



(b)

$$\overline{\chi_r(\mathbf{x})} = \int_{\mathcal{E}} \chi_r(\mathbf{x}; \alpha) p(\alpha) d\alpha, \quad (2)$$

where $p(\alpha)$ is a probability density function. The n -point probability function, $S_{r_1 r_2 \dots r_n}(\mathbf{x}_1, \mathbf{x}_2, \dots, \mathbf{x}_n)$, is defined as

$$S_{r_s \dots r_q}(\mathbf{x}_1, \mathbf{x}_2, \dots, \mathbf{x}_n) = \overline{\chi_{r_s}(\mathbf{x}_1) \chi_{r_s}(\mathbf{x}_2) \dots \chi_{r_q}(\mathbf{x}_n)}, \quad (3)$$

and it represents the probability of finding phases r, s, \dots, q at points $\mathbf{x}_1, \mathbf{x}_2, \dots, \mathbf{x}_n$ simultaneously.

The probability functions for a heterogeneous material are spatially complex in general. If the material satisfies ergodicity, statistical homogeneity, and isotropy, the ensemble average can be replaced by the volume average and the probability functions are translation and direction invariant [42]. With these three simplifications, the one-point probability function is reduced to the volume fraction, and the higher-order probability functions depend on the distance only,

$$S_r(\mathbf{x}) = c_r,$$

$$S_{rs}(\mathbf{x}, \mathbf{x}') = S_{rs}(|\mathbf{x} - \mathbf{x}'|),$$

$$S_{rsq}(\mathbf{x}, \mathbf{x}', \mathbf{x}'') = S_{rsq}(|\mathbf{x} - \mathbf{x}'|, |\mathbf{x} - \mathbf{x}''|), \quad (4)$$

where c_r is the volume fraction of the phase r . We also observe the limit cases of the two- and three-point probability functions which can be expressed as

$$S_{rs}(\mathbf{x}, \mathbf{x}') \rightarrow \begin{cases} c_r \delta_{rs} & \text{if } |\mathbf{x} - \mathbf{x}'| \rightarrow 0 \\ c_r c_s & \text{if } |\mathbf{x} - \mathbf{x}'| \rightarrow \infty, \end{cases} \quad (5)$$

$$S_{rsq}(\mathbf{x}, \mathbf{x}', \mathbf{x}'') \rightarrow \begin{cases} c_r \delta_{rs} \delta_{rq} & \text{if } |\mathbf{x} - \mathbf{x}'|, |\mathbf{x} - \mathbf{x}''| \rightarrow 0 \\ S_{rq}(\mathbf{x}, \mathbf{x}'') & \text{if } |\mathbf{x} - \mathbf{x}'| \rightarrow 0 \\ c_r c_s c_q & \text{if } |\mathbf{x} - \mathbf{x}'|, |\mathbf{x} - \mathbf{x}''| \rightarrow \infty, \end{cases} \quad (6)$$

where δ_{rs} is the Kronecker delta.

B. Morphology of a pack

To obtain the statistical properties of the pack that is based on the voxel pack as discussed in Sec. II, we discretize the probability space. The probability functions are numerically sampled through a Monte Carlo–like method. A spherical sampling template depicted in Fig. 4 is used. This template is especially advantageous for isotropic cases as pointed out in [43]. The probability functions described in

FIG. 5. (Color online) (a) Polydisperse pack obtained from the voxel pack by replacing voxel-based inclusions with spheres. Each color of particle in the pack belongs to a different mode according to pdf shown in Fig. 3(a). (b) The corresponding one-point probabilities (volume fractions).

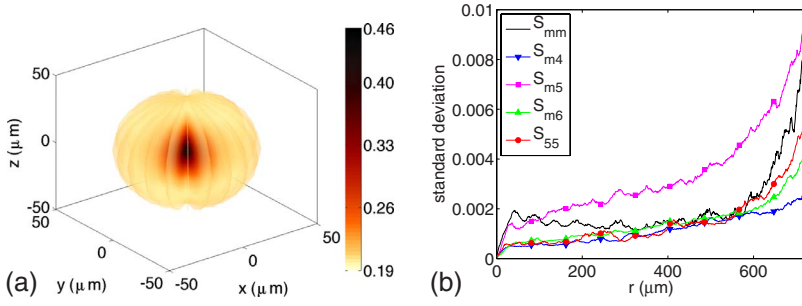


FIG. 6. (Color online) (a) Full two-point probability function S_{mm} . Observe the sphericity of S_{mm} with the value at the origin converging to the volume fraction and value at infinity converging to c_m^2 . (b) The corresponding standard deviation of isotropy, $\sigma_{S_{rs}}$, for selected second-order probability functions. Although the standard deviation is small over the whole x range, observe the increase of $\sigma_{S_{rs}}$ due to the wall effect.

Sec. III A are computed by our parallel code, STAT3D, allowing for a large domain to be efficiently evaluated [36]. For the present pack, we sample the one- and two-point probability functions by throwing a sampling template with 1000 radial points and 20 circumferential points 500 000 times. These sampling parameters have been selected after a convergence study to assure the spatial convergence.

The one-point probabilities (volume fractions) of the pack are shown in Fig. 5(b). The nine bins are based on those of the probability density function plotted in Fig. 3(a) and each bin is assigned a different mode number (1–9). For the total volume to be conserved, one has $\sum_1^N c_i = 1$, where N represents the total number of phases. In our case, $N = 10$ including the matrix (m) (voids in the prepared pack). We evaluate $c_m = 0.46$ numerically for our particulate medium, which is different from $1 - \sum_1^{N_p} c_i$ by 0.2%, where N_p is the number of the particle modes ($N_p = N - 1$). However, considering the image resolution ($2.818 \mu\text{m}$ voxel) and the error due to the separation procedure (2.1% in the total packing fraction), the volume conservation error is well controlled.

Figure 6(a) shows the two-point probability function, S_{mm} , zoomed at the core in the four-dimensional space. The colored sphere shows the probability of finding the phase m (matrix) when its center lies in the matrix as well. We find that the two-point probability functions of the pack satisfy isotropy with the standard deviation, $\sigma_{S_{rs}}$, remaining less than 1% of the magnitude of the actual probability function, shown in Fig. 6(b). The exponential behavior of the deviation at the large radii can be attributed to the wall effect, which produces a significantly different packing structure

near the boundary of the container as pointed out in [9,44]. Based on the observation of isotropy, we can average the two-point probability functions over all the possible orientations since it is direction invariant. Statistical homogeneity and ergodicity of the particulate composites under consideration have been verified in [45]. In Fig. 7, the isotropic two-point probability functions and their gradients are shown. We note that the isotropic two-point probability functions saturate when the radius is greater than $200 \mu\text{m}$, which provides a characteristic material length scale, i.e., the optimal size of a unit cell: twice the radius or $400 \mu\text{m}$. Note that there are 100 two-point probability functions in our computations since we have ten different phases (the nine particle modes and the matrix). Figure 7 shows only five selected second-order probability functions. However, the trends are the same for the other second-order probability functions.

To validate the probability functions evaluated on the pack, we use the limit cases of the second-order probability functions in Eq. (5), i.e., the two-point probability functions are examined for convergence to one-point probability functions in the limit cases and for numerical error due to sampling. In order to quantify the physical errors for the pack, we define two error functions for two-point probabilities,

$$\varepsilon_{S_{rs}(0,0)} = |S_{rs}(0,0) - c_r \delta_{rs}|, \tag{7}$$

$$\varepsilon_{S_{rs}(0,\infty)} = |S_{rs}(0,\infty) - c_r c_s|. \tag{8}$$

In our analysis, we have maximum errors of 0.001 and 0.004 over the 100 two-point probability functions, measured by

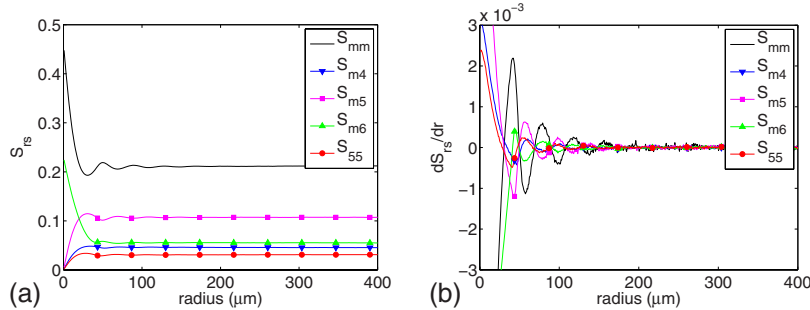


FIG. 7. (Color online) (a) Isotropic two-point probability functions S_{rs} computed by radial averaging of complete probability functions in Fig. 6(a). Only selected S_{rs} functions are shown for clarity. Note that probability functions are plotted for radius $\leq 400 \mu\text{m}$ to make their behavior close to the origin more visible. However, full probability functions are computed for radius $723 \mu\text{m}$ [one-half of the longest edge of the pack in Fig. 5(a)]. Detailed structure of S_{rs} governed by spatial interactions of particles and their corresponding diameters can be seen. (b) Gradients of S_{rs} . The gradients of the two-point probability functions show where the functions reach the asymptotic values. This distance provides a characteristic material length scale of the second order, and we use it to construct the size of the RUC.

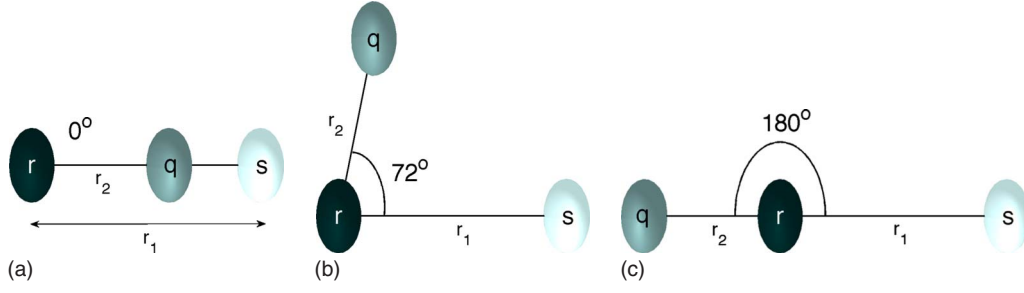


FIG. 8. (Color online) Alignments of three points in phases r , s , and q . (a) $\theta=0^\circ$. (b) $\theta=72^\circ$. (c) $\theta=180^\circ$.

expressions (7) and (8), respectively. Given that $\varepsilon_{S_{rs}(0,0)}$ and $\varepsilon_{S_{rs}(0,\infty)}$ range in $[0,1]$, these errors are negligible. The numerical error is calculated by

$$\varepsilon_{S_{sr}|S_{rs}} = \frac{\|S_{rs} - S_{sr}\|_{L_2^D}}{\sum_{r=1}^N \sum_{s=1}^N \|S_{rs}\|_{L_2^D}/N^2}, \quad (9)$$

where $\|\cdot\|_{L_2^D}$ is the discrete L_2 norm and N represents the number of phases. Since S_{rs} and S_{sr} are symmetric, $\varepsilon_{S_{sr}|S_{rs}}$ represents a relative numerical error. For the current pack, the maximum value of the error based on Eq. (9) is 0.035 and the mean is 0.006. This error criterion provides confidence in the spatial convergence of our analysis.

For many physical processes, the higher-order statistics play an important role in capturing the interactions between particles, such as a case where a small particle lies between two big particles. For example, such a scenario helps to promote decohesion. Therefore, we also investigate three-point probability functions. As expected, the three-point probability functions tend to be more sensitive to the geometrical properties of a pack than the two-point probability functions. We recall that the three-point probability functions depend on two vectors in general. Thus, the function $S_{rsq}(\mathbf{x}-\mathbf{x}', \mathbf{x}-\mathbf{x}'')$ is defined in a seven-dimensional space, considering two vectors in three dimensions and the function value itself. Since the numerical evaluation of the full three-point probability function is computationally expensive, we use a semi-isotropic assumption in terms of the orientation of a plane determined by the two randomly gen-

erated vectors. This assumption reduces the space dimensionality from seven to four since $S_{rsq}(\mathbf{x}-\mathbf{x}', \mathbf{x}-\mathbf{x}'')$ becomes $S_{rsq}(|\mathbf{x}-\mathbf{x}'|, |\mathbf{x}-\mathbf{x}''|, \theta)$, where θ is the angle between the two vectors $\mathbf{x}-\mathbf{x}'$ and $\mathbf{x}-\mathbf{x}''$. We again use the sampling template, shown in Fig. 4, and average on planes generated by discrete rays (semi-isotropy). Note that for the perfectly statistically isotropic material, the three-point probability functions are angle independent except when they degenerate to the lower-order probability functions,

$$S_{rsq} \rightarrow \begin{cases} S_{rs}\delta_{rq} & \text{on } r_1 \text{ axis} \\ S_{rq}\delta_{rs} & \text{on } r_2 \text{ axis} \\ S_{rs}\delta_{sq} & \text{on } r_1=r_2, \end{cases} \quad (10)$$

where $r_1=|\mathbf{x}-\mathbf{x}'|$ and $r_2=|\mathbf{x}-\mathbf{x}''|$.

There are 1000 different three-point probability functions for a ten-phase medium. However, due to the symmetries, $S_{rs}=S_{sr}$, $S_{rsq}=S_{rq s}$, etc., several functions can be omitted. In this work, we do not investigate all third-order probabilities and rather focus on the generic findings that are typical for the third-order statistics. Thus, we present symmetric and unsymmetric types of the three-point probability functions. To compute the third-order statistics of the pack, we use 50 000 throws of a template with 1000 radial and 20 circumferential points. Sampling accuracy is again determined by the limit cases in Eq. (10). Figure 8 shows the different arrangements of the three randomly generated points in phases r , s , and q for S_{rsq} at the three different angles, 0° , 72° , and 180° , for instance. For a symmetric case, S_{355} is selected to represent the $S_{rs s}$ type of three-point probability functions. Figure 9 shows S_{355} at the three angles mentioned above.

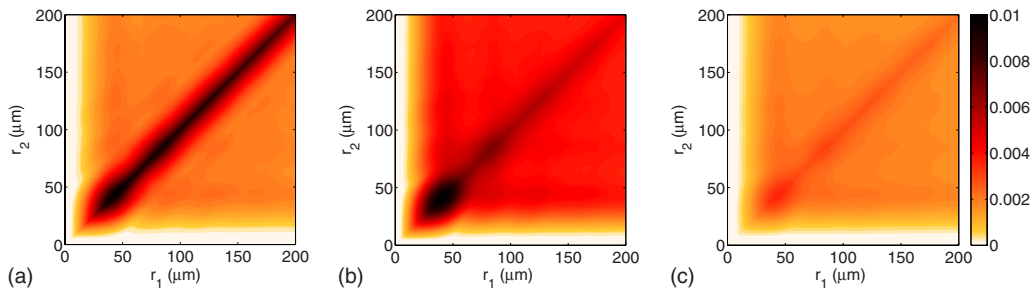


FIG. 9. (Color online) Three-point probability function S_{355} of the pack depicted in Fig. 5(a). A diagram of S_{rsq} computation is shown in Fig. 8. We use a semi-isotropic assumption in evaluation of S_{rsq} . (a) S_{355} for $\theta=0^\circ$. Note the symmetric degeneracy of $S_{355} \rightarrow S_{35}$ on $r_1=r_2$ ray for $\theta=0^\circ$. (b) S_{355} for $\theta=72^\circ$. (c) S_{355} for $\theta=180^\circ$. A certain degree of anisotropy in third-order statistics can be observed for (b) and (c) since for a perfectly isotropic medium $S_{rsq}(|\mathbf{x}-\mathbf{x}'|, |\mathbf{x}-\mathbf{x}''|)$ is an angle θ independent except for degenerate cases [Eq. (10)] as shown in (a).

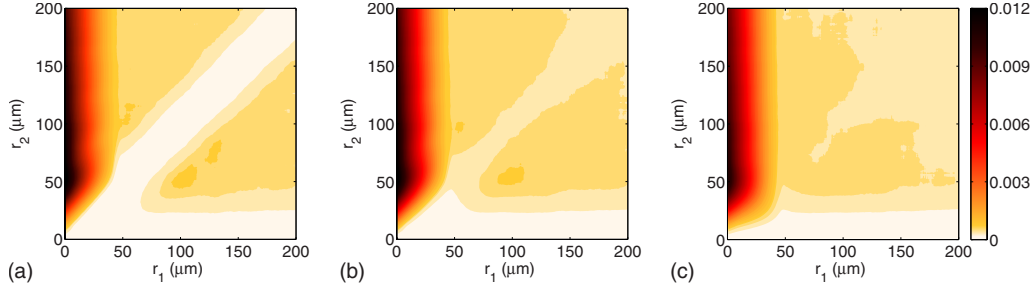


FIG. 10. (Color online) Three-point probability function S_{775} of the pack depicted in Fig. 5(a). (a) S_{775} for $\theta=0^\circ$. Note the nonsymmetric degeneracy of $S_{775} \rightarrow S_{75}$ on r_2 axis for $\theta=0^\circ$. (b) S_{775} for $\theta=72^\circ$. (c) S_{775} for $\theta=180^\circ$.

Since s and q are the same in this case, S_{355} comes to zero on both r_1 and r_2 axes, while it degenerates to S_{35} for $r_1 \equiv r_2$ [Eq. (10)]. Figure 10 shows an unsymmetric three-point probability function S_{775} which goes to zero on r_1 axis and $r_1 \equiv r_2$ while it converges to S_{75} on r_2 axis. In Figs. 9 and 10, the widths of the three characteristic bands at $\theta=0^\circ$ depend on the sizes of the particles in the bins r , s , and q of S_{rsq} . Even though the present pack is almost isotropic based on the two-point probability functions, the three-point probability still captures some anisotropic aspects of the pack, showing some dependency on angles. We will return to elaborate on the anisotropy and on the degeneracy of the third-order statistics in Sec. IV B.

IV. RECONSTRUCTION OF A REPRESENTATIVE UNIT CELL

In this section, we proceed to construct the RUC that retains the statistical characteristics of the pack shown in Fig. 5(a). The two main steps in the reconstruction are to find the length scale of the RUC and to optimally locate the particles with a minimum (or no) particle overlap. Finally, the statistical results of the cell are compared with those of the pack.

A. Numerical method

First, let us recall the two-point probability functions in Fig. 7. The two-point probability functions depend only on the distance since the material satisfies both the statistical isotropy and homogeneity assumptions. We also observe that the functions start to reach the asymptotic values at 200 μm

which is a good candidate for the size of the unit cell (h_0).

With this initial guess on the length scale of the cell, we minimize two objective functions which reflect the differences of the one- and two-point probability functions between the pack and the cell. For $0 \leq h \leq h_0$, the first objective function is defined as

$$\mathcal{F}_1(h) = \sqrt{\sum_{i=1}^{N_p} (c_i^p - c_i^c)^2} = \sqrt{\sum_{i=1}^{N_p} \left(c_i^p - \frac{4\pi r_i^3 n_i}{3h^3} \right)^2}, \quad (11)$$

where c_i^p , c_i^c , r_i , and n_i are the volume fraction of the pack, the volume fraction of the cell, the particle radius, and the total number of particles in phase i , respectively. By finding the local minimum of the first objective function, we can determine the optimal length scale (h_c) of the cell as

$$\frac{d\mathcal{F}_1(h)}{dh} = 0 \Rightarrow h_c = \left(\frac{4\pi \sum_{i=1}^{N_p} n_i^2 r_i^6}{3 \sum_{i=1}^{N_p} c_i^p N_i r_i^3} \right)^{1/3}. \quad (12)$$

To construct the second objective function, we first consider a functional which represents the difference of the two-point probability functions between the pack and the cell,

$$\mathcal{F}_2(\mathbf{x}_n) = \sum_{r=1}^N \sum_{s=1}^N \|S_{rs}^p - S_{rs}^c\|_{L^2}, \quad (13)$$

where \mathbf{x}_n is the position vector of all particle centers \mathbf{x}_r . To avoid the overlap between particles, we impose a constraint on Eq. (13),

TABLE I. Comparison of the raw fitness \mathcal{F}_2 in Eq. (13) before and after performing the genetic algorithm for the five reconstructed cells. The number of GA iterations for convergence and the overall particle overlap are also shown.

Pack No.	\mathcal{F}_2 before GA			\mathcal{F}_2 after GA			No. of iteration	Overlap
	Min	Mean	Max	Min	Mean	Max		
Run 1	4.035	7.253	10.963	0.520	0.606	0.839	578	0.000%
Run 2	4.202	7.600	11.348	0.581	0.774	1.163	942	0.001%
Run 3	3.993	7.537	11.179	0.590	0.773	1.253	807	0.002%
Run 4	3.989	7.335	10.801	0.587	0.652	0.793	1452	0.000%
Run 5	4.075	7.420	11.128	0.535	0.574	0.699	1726	0.000%

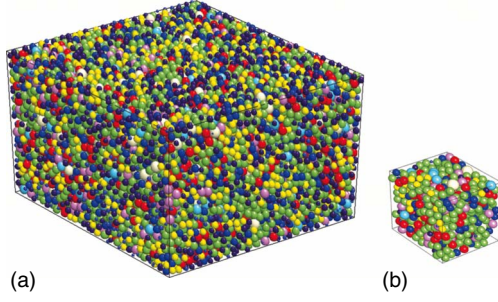


FIG. 11. (Color online) (a) The pack contains 19 123 particles in $1445.372 \times 1287.892 \times 789.106 \mu\text{m}^3$. (b) The reconstructed cell is composed of 1082 particles in $399.632 \times 399.632 \times 399.632 \mu\text{m}^3$.

$$\sqrt{(\mathbf{x}_i - \mathbf{x}_j)^2} \geq r_i + r_j, \quad \forall i = 1, \dots, n-1, \quad \forall j = i + 1, \dots, n, \quad (14)$$

where n is the total number of particles in the cell ($n = \sum_{i=1}^N n_i$) and r_i and r_j are the radii of i th and j th particles, respectively. The number of particles in the cell is calculated based on the ratio of the volume of the pack and that of the cell from the initial guess. Note that only a whole particle,

not its fraction, can be added into a particular particle mode in the cell.

The raw objective function and the constraint can be combined to construct an overall objective function or a fitness function, \mathcal{F} , which yields

$$\mathcal{F} = \frac{\sum_{r=1}^N \sum_{s=1}^N \|S_{rs}^p - S_{rs}^c\|_{L_2^D}}{N \cdot N} + p. \quad (15)$$

$$\max_{\mathcal{P}_0} \sum_{r=1}^N \sum_{s=1}^N \|S_{rs}^p - S_{rs}^c\|_{L_2^D}$$

The denominator in the first term of Eq. (15) represents the value of the objective function \mathcal{F}_2 of the worst sample pack in the initial population \mathcal{P}_0 and p is a penalty function in the range $[0,1]$ that is used to enforce the constraint [Eq. (14)]. We also use the mass-spring dynamic mutation operator to eliminate the overlap as discussed in [36]. This fitness function is multimodal with multiple local minima. To minimize this function, we use the augmented simulated annealing technique, a stochastic optimization method based on the principle of evolution, such as genetic algorithms (GAs) combined with SA, introduced in [46]. The genetic algorithm is briefly described in Algorithm 1.

Algorithm 1: Principle of genetic algorithm.

- 1 $g=0$
- 2 generate and evaluate population \mathcal{P}_g of size N_i
- 3 **while** (not termination-condition) {
- 4 select m individuals to \mathcal{M}_g from \mathcal{P}_g (apply sampling mechanism)
- 5 alter \mathcal{M}_g (apply genetic operators)
- 6 create and evaluate \mathcal{P}_{g+1} from \mathcal{M}_g (insert m new individuals into \mathcal{P}_{g+1})
- 7 $g=g+1$
- 8 }

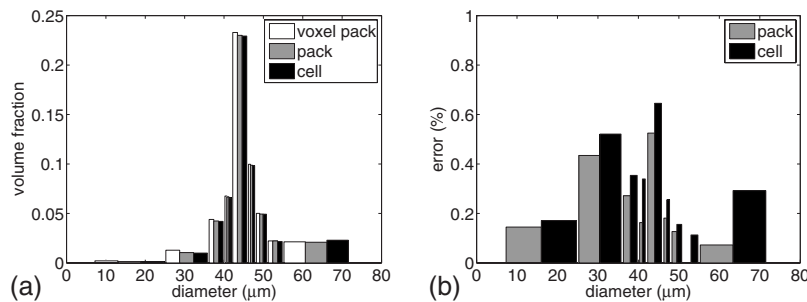


FIG. 12. (a) Volume fractions of each bin for the voxel pack, the pack, and the cell. The voxel pack values are computed directly from voxels, whereas the pack and cell values are computed by statistical sampling. (b) Relative error in volume fraction for each bin as given by Eq. (16). Errors in volume fractions between the voxel pack and the pack, which are the consequence of mapping voxel-based inclusions to spheres, are smaller than those between the voxel pack and the cell since the cell is geometrically smallest possible object for a given finite number of whole particles.

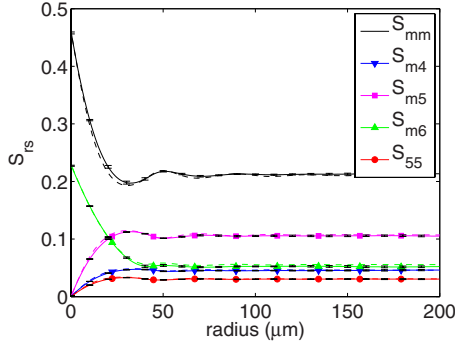


FIG. 13. (Color online) Comparison of the averaged two-point probability functions between the pack (dotted lines) and the cell (solid lines). Average values are computed from five optimization runs as given in Table I. Note the very small error bars. Only selected probability functions are plotted.

For our optimization problem, the population \mathcal{P}_g in the Algorithm 1 becomes a family of possible cell configurations with particles of fixed diameters, which are distributed according to the rebinned pdf (Fig. 3) placed inside the cell. The unknowns are positions of the particle centers \mathbf{x}_i [see Eq. (13)] in the Algorithm 1. These methods were previously implemented into our code, RECON3D, which reconstructs the unit cell in parallel, preserving the end-to-end parallelism and allowing for the optimal computational domain to be generated quickly [36] (see [35,36] for more details on the optimization process).

B. Comparison of statistical properties between pack and cell

To establish the robustness of the proposed reconstruction method, we run RECON3D on 2048 CPUs and reconstruct five different statistically optimal cells. We note now that periodic conditions are enforced on the cell boundary, i.e., all particles intersected by the bounding box have periodic replicas (two if a particle is on a face, four if a particles in on an edge, and eight if a particle sits in a corner). Periodic boundary conditions are extensively used in computational studies due to their simplicity, reasonable physical relevance, and deep mathematical foundation [47]. Thus, a nonperiodic voxel medium is mapped to a statistically equivalent periodic RUC. All the runs consist of a population of $N_i=512$ indi-

viduals and there are $m=16$ individuals in the mating pool, \mathcal{M} [pool where genetic operators are applied (see Algorithm 1)]. During the initialization of the genetic algorithm, one-half of the individuals in the population is generated randomly, i.e., all particles with fixed diameters are placed in the cell of dimensions h_c without overlap considerations. The other half is generated using ballistic deposition, i.e., a randomly deposited particle is checked for overlap and this process is repeated until all particles are placed successfully, allowing only a certain degree of overlap. Each reconstruction simulation is stopped when the maximum number of iterations (10 000) is reached or when the best individual set is not improved for 300 generations. In Table I, we compare the raw fitness \mathcal{F}_2 before and after running the genetic algorithm. As one can see, a large improvement in the fitness after optimization has been obtained. The fitness after the genetic algorithm was improved by 91% on average. The final number of iterations needed for convergence and the overall particle overlap are also shown.

Figure 11 shows the comparison of the dimensions of the pack and one particular RUC. The pack includes 19 123 particles in $1445.372 \times 1287.892 \times 789.106 \mu\text{m}^3$ as mentioned previously, while the unit cell has 1082 particles in $399.632 \times 399.632 \times 399.632 \mu\text{m}^3$. These numbers highlight the substantial reduction of the computational space.

We now assess the quality of the reconstruction for both the first- and the second-order probability functions. First, we average the one-point probability functions over the five cells. The averaged one-point probabilities of the five cells are compared with those of the voxel pack and the pack in Fig. 12(a). The maximum standard deviation for the sampled volume fractions is less than 0.003 (bin 9) and is not displayed. The corresponding relative error (ϵ_i^q) of the volume fraction in the i th bin between the voxel pack and the pack and/or the cell is calculated by

$$\epsilon_i^q(\%) = \frac{|c_i^v - c_i^q|}{\sum_{i=1}^{N_p} c_i^v} \times 100, \tag{16}$$

where c_i^v is the i th bin's volume fraction of the voxel pack and q is either p (pack) or c (cell). As seen in Fig. 12(b), the error is less than 0.8% for both the pack and the cell.

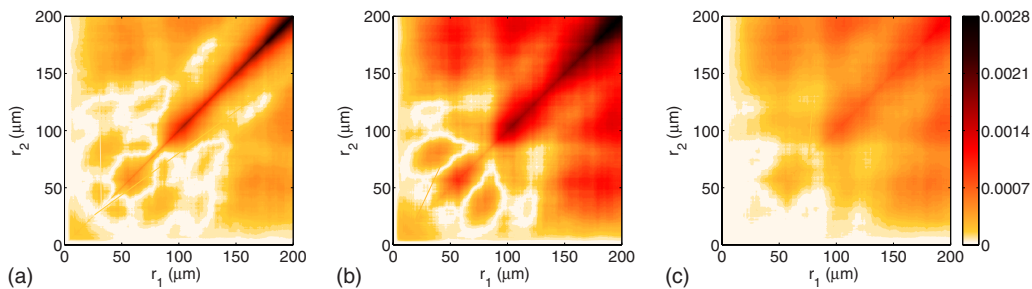


FIG. 14. (Color online) The difference, $|S^p_{355} - S^c_{355}|$, between the pack and the cell for several angles θ . (a) The difference for $\theta=0^\circ$. (b) The difference for $\theta=72^\circ$. (c) The difference for $\theta=180^\circ$. Note that the saturation value for S_{355} is ~ 0.01 on $r_1=r_2$ ray at $\theta=0^\circ$, and thus, the errors depicted above are of $\sim 28\%$. Also note that the largest errors are obtained at the unit cell boundaries for $r_1 \rightarrow h_c$ and $r_2 \rightarrow h_c$, where h_c is the size of the RUC. The degenerate case for S_{355} is depicted in Fig. 16.

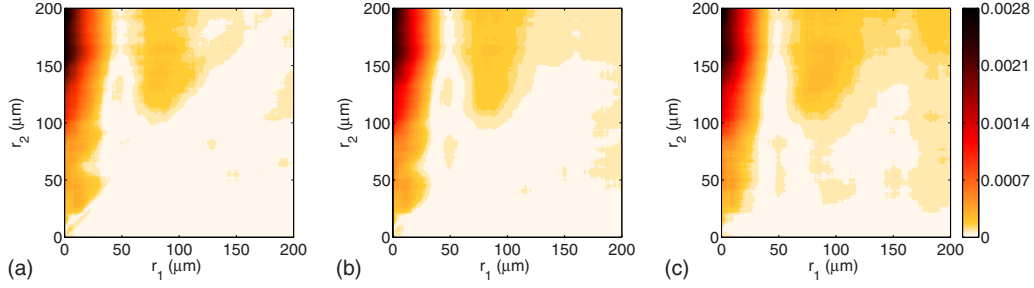


FIG. 15. (Color online) The difference, $|S_{775}^p - S_{775}^c|$, between the pack and the cell for several angles θ . (a) The difference for $\theta=0^\circ$. (b) The difference for $\theta=72^\circ$. (c) The difference for $\theta=180^\circ$. Note that the saturation value for S_{775} is ~ 0.012 on $r_1=0$ ray at $\theta=0^\circ$, and thus, the errors depicted above are of $\sim 23\%$. Also note that the largest errors are obtained at the unit cell boundaries for $r_1=0$ and $r_2 \rightarrow h_c$, where h_c is the size of the RUC. The degenerate case for S_{775} is depicted in Fig. 17.

Next, we focus on the second-order statistics. One of the error measures is provided directly by the objective function \mathcal{F}_2 itself [Eq. (13)]. Note that we optimized the full probability spectrum composed of 100 second-order probability functions for this example. The comparison of the isotropic two-point probability functions between the pack and the cell is presented in Fig. 13. The error bars in Fig. 13 represent the standard deviations of the two-point probability functions computed on the five cells. Note that the error bars contain both the numerical (sampling) and the physical (statistics of five cells) error components. To assess the relative error, the difference of the two-point probability functions between the pack and the cell is calculated by

$$\mathcal{E}(\%) = \frac{\sum_{r=1}^N \sum_{s=1}^N \|S_{rs}^p - S_{rs}^c\|_{L_2^D}}{\sum_{r=1}^N \sum_{s=1}^N (\|S_{rs}^p\|_{L_2^D} + \|S_{rs}^c\|_{L_2^D})/2} \times 100, \quad (17)$$

where S_{rs}^c is the averaged isotropic two-point probability function over the five cells. In the present case we have excellent agreement with only 0.0387% error. Assuming the uniform distribution of the error for all 100 second-order probability functions, the error measure [Eq. (13)] yields a very small inaccuracy of ~ 0.006 between S_{rs}^p of the pack and S_{rs}^c of the cell over the length of $\sim 200 \mu\text{m}$. This is a remarkable resolution for the full second-order probability spectrum, manifested by almost coincident lines in Fig. 13, and

this would hold for all the other second-order probability functions as well.

Even though the unit cell is reconstructed based on the one- and two-point probability functions, we also investigate the three-point probability functions. The three-point probability function of the cell, S_{rsq}^c , is compared with that of the pack, S_{rsq}^p , by calculating the difference, $|S_{355}^p - S_{355}^c|$, for $(r, s, q) = (3, 5, 5), (7, 7, 5)$ corresponding to Figs. 9 and 10. Figures 14 and 15 show the differences at the three different angles, 0° , 72° , and 180° , depicted in Fig. 8 for these two cases, respectively. The difference of the three-point probability between the pack and the cell is noticeable in comparison to the good agreement of the lower-order probability functions, which indicates that optimization of the three-point probability functions would be desirable.

In Figs. 16 and 17, we further compare the three-point probability functions, S_{355} and S_{775} , with the two-point probability functions S_{35} and S_{75} . We recall the convergence of the three-point probability function at the second limit case in Eq. (6), which states that the third-order function degenerates to the second-order one at the angle 0° , where $r_1=r_2$ for S_{355} and $r_1=0$ for S_{775} .

The two- and the three-point probability results produced for the pack do not come to agreement, whereas those for the cell do. This discrepancy can be attributed not only to the periodicity imposed on the cell boundary and lack thereof in the case of the pack, but also to the strict enforcement of the statistical isotropy, given by Eq. (13), in the cell reconstruction, which is not enforced for the pack statistics. To investigate this discrepancy further, let us recall that we compute

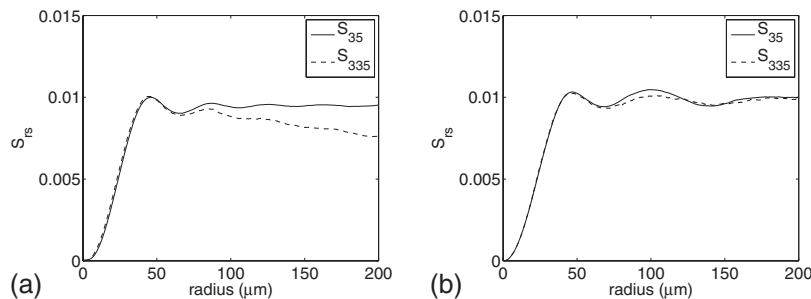


FIG. 16. Comparison between the two-point probability function S_{35} (solid line) and the degenerated S_{355} (dashed line) on $r_1=r_2$ ray at $\theta=0^\circ$. (a) Comparison computed for the pack. (b) Comparison computed for the cell. Note that S_{35} is computed to be statistically isotropic, whereas S_{355} is not. Thus, for the pack (a) we observe an anisotropy in the third order, whereas the RUC (b) is fairly isotropic.

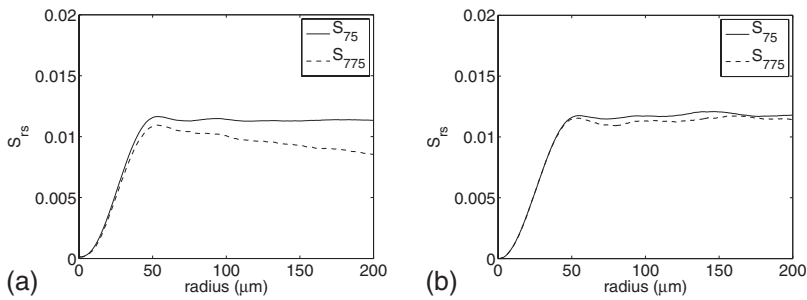


FIG. 17. Comparison between the two-point probability function S_{75} (solid line) and the degenerated S_{775} (dashed line) on r_2 axis at $\theta=0^\circ$. (a) Comparison computed for the pack. (b) Comparison computed for the cell. Note that S_{75} is computed to be statistically isotropic, whereas S_{775} is not. Thus, for the pack (a) we observe an anisotropy in the third order, whereas the RUC (b) is fairly isotropic.

S_{rsq} by assuming the semi-isotropic assumption leaving θ as an extra variable to account for anisotropy, while S_{rs} is averaged over all possible orientations in the cell reconstruction. Figures 16(a) and 17(a) indicate that the pack is anisotropic (see also Figs. 9 and 10) in third-order statistics since the degenerate cases are not recovered for the numerically converged solution. On the other hand, the degenerate cases for the cell [Figs. 16(b) and 17(b)] are well established. This finding suggests that the cell structure is less ordered than that of the pack, which has some third-order directional variance (anisotropy) (see also Figs. 9 and 10). The reasons for more randomness in the cell morphology as contrasted to the pack one are our objective function [Eq. (13)] that strictly enforces the statistical isotropy (directional invariance) and the periodic boundary conditions that mimic an infinite medium as opposed to a closed pack with wall effects. Note that the characteristic material length scale, h_c , established in this work is of the second-order only and that the third-order bound would possibly require a larger window of observation.

V. CONCLUSIONS

The paper describes a reconstruction procedure for statistically optimal representative unit cells from rich three-dimensional tomographic data. The particulate composite under investigation consists of glass beads packed in a cylindrical container. High resolution microtomography is employed to gather the material data, and the image recognition software AMIRA is used for data processing. The first-, second-, and third-order probability functions are used to characterize a polydisperse particulate medium. Error measures are established to assess the quality of the statistical characterization. A fully represented probability spectrum is optimized without distortion of the particle shape and with a constraint on the particle overlap, furnishing the resulting minimization problem highly complex with several local minima. Therefore, the parallel augmented simulated annealing technique is employed to solve the optimization problem on massively parallel computers. Presented results show

good repeatability of the reconstruction procedure. Excellent agreement is obtained for statistics of the voxel-based pack and statistics of the reconstructed unit cell.

Investigation of the higher-order probability functions reveals disagreement in the third-order probabilities between the pack and the cell even though the first- and second-order functions are well optimized. Thus, potential extension of this work is in expansion of the fitness function for the third-order statistics. Also, optimization of polydisperse composites with different inclusion shapes, such as ellipsoids, rhombi, etc., is of interest.

It is important to note that the reconstructed unit cells are only representative from a geometrical statistics point of view and that the representativity of the unit cell must also account for the physical processes of interest, such as mechanical or transport properties. However, the construction of a geometrically equivalent representative unit cell is an important first step in describing behavior of complex heterogeneous materials, and both computational and experimental evidences suggest that a statistical approach adopted in this work accounts for the most important interactions [48,49]. Moreover, advances in parallel computing are making fully resolved simulations of complex physical phenomena, such as combustion [50], on cells presented in this work a reality.

ACKNOWLEDGMENTS

The authors would like to gratefully acknowledge the support from the Center for Simulation of Advanced Rockets at the University of Illinois under Contract No. B523819 by the (U.S.) Department of Energy as a part of its Advanced Simulation and Computing program. K.M. and H.L. would like to also acknowledge the support from Buckmaster Research-DoD STTR program, USAFOSR. Moreover, the authors thank Michael Campbell for running the reconstruction code on Red Storm computer located at Sandia National Laboratories, NM, and to Sergei Poliakov for running the statistics code on the Turing cluster. Finally, the authors gratefully acknowledge the use of the Turing cluster maintained and operated by the Computational Science and Engineering Program at the University of Illinois.

- [1] S. V. Kochevets, T. L. Jackson, J. Buckmaster, and A. Hegab, *Journal of Propellant and Power* **17**, 883 (2001).
- [2] K. Matouš, H. M. Inglis, X. Gu, D. Rypl, T. L. Jackson, and P. H. Geubelle, *Compos. Sci. Technol.* **67**, 1694 (2007).
- [3] J. E. Andrade and X. Tu, *Mech. Mater.* **41**, 652 (2009).
- [4] J. Liang and K. A. Dill, *Biophys. J.* **81**, 751 (2001).
- [5] P. M. Chaikin and T. C. Lubensky, *Principles of Condensed Matter Physics* (Cambridge University Press, New York, 2000).
- [6] C. E. Shannon, *Bell Labs Technical Journal* **27**, 379 (1948).
- [7] J. H. Conway and N. J. A. Sloane, *Sphere Packings, Lattices, and Groups* (Springer, New York, 1987).
- [8] Y. Jiao, F. H. Stillinger, and S. Torquato, *Phys. Rev. E* **79**, 041309 (2009).
- [9] F. Maggi, S. Stafford, T. L. Jackson, and J. Buckmaster, *Phys. Rev. E* **77**, 046107 (2008).
- [10] X. Jia and R. A. Williams, *Powder Technol.* **120**, 175 (2001).
- [11] S. Gallier and F. Hiernard, *J. Propul. Power* **24**, 147 (2008).
- [12] B. C. Collins, F. Maggi, K. Matouš, T. L. Jackson, and J. Buckmaster, "In 46th AIAA Aerospace Sciences Meeting and Exhibit," AIAA Paper No. 2008-941 (2008).
- [13] T. Aste, M. Saadatfar, and T. J. Senden, *Phys. Rev. E* **71**, 061302 (2005).
- [14] S. Rolland du Roscoat, M. Decain, X. Thibault, C. Geindreau, and J.-F. Bloch, *Acta Mater.* **55**, 2841 (2007).
- [15] D. Bouvard, J. M. Chaix, R. Dendievel, A. Fazekas, J. M. Ltang, G. Peix, and D. Quenard, *Cem. Concr. Res.* **37**, 1666 (2007).
- [16] J. D. Bernal, *Nature (London)* **183**, 141 (1959).
- [17] M. B. Weissman, *Annu. Rev. Mater. Res.* **26**, 395 (1996).
- [18] J. Schmalzing and K. M. Gorski, *Mon. Not. R. Astron. Soc.* **297**, 355 (1998).
- [19] P. Wochner, C. Gutt, T. Autenrieth, T. Demmer, V. Bugaev, A. D. Ortiz, A. Duri, F. Zontone, G. Grüel, and H. Dosch, *Proc. Natl. Acad. Sci. U.S.A.* **106**, 11511 (2009).
- [20] P. Areias and K. Matouš, *Comput. Methods Appl. Mech. Eng.* **197**, 4702 (2008).
- [21] K. Matouš and P. H. Geubelle, *Int. J. Numer. Methods Eng.* **65**, 190 (2006).
- [22] G. L. Povirk, *Acta Metall. Mater.* **43**, 3199 (1995).
- [23] C. L. Y. Yeong and S. Torquato, *Phys. Rev. E* **57**, 495 (1998).
- [24] C. L. Y. Yeong and S. Torquato, *Phys. Rev. E* **58**, 224 (1998).
- [25] B. Bochenek and R. Pyrz, *Comput. Mater. Sci.* **31**, 93 (2004).
- [26] J. Zeman and M. Šejnoha, *Modell. Simul. Mater. Sci. Eng.* **15**, S325 (2007).
- [27] Y. Jiao, F. H. Stillinger, and S. Torquato, *Phys. Rev. E* **76**, 031110 (2007).
- [28] Y. Jiao, F. H. Stillinger, and S. Torquato, *Phys. Rev. E* **77**, 031135 (2008).
- [29] D. T. Fullwood, S. R. Niezgoda, and S. R. Kalidindi, *Acta Mater.* **56**, 942 (2008).
- [30] G. T. Seidler, G. Martinez, L. H. Seeley, K. H. Kim, E. A. Behne, S. Zaranek, B. D. Chapman, S. M. Heald, and D. L. Brewster, *Phys. Rev. E* **62**, 8175 (2000).
- [31] C. H. Arns, M. A. Knackstedt, and K. R. Mecke, *Phys. Rev. Lett.* **91**, 215506 (2003).
- [32] K. R. Mecke and C. H. Arns, *J. Phys.: Condens. Matter* **17**, S503 (2005).
- [33] V. Sundararaghavan and N. Zabaras, *Comput. Mater. Sci.* **32**, 223 (2005).
- [34] J. A. Quintanilla and W. Max Jones, *Phys. Rev. E* **75**, 046709 (2007).
- [35] N. C. Kumar, K. Matouš, and P. H. Geubelle, *Comput. Mater. Sci.* **42**, 352 (2008).
- [36] B. C. Collins, K. Matouš, and D. Rypl, *Int. J. Multiscale Comp. Eng.* (to be published).
- [37] E. R. Nowak, J. B. Knight, E. Ben-Naim, H. M. Jaeger, and S. R. Nagel, *Phys. Rev. E* **57**, 1971 (1998).
- [38] K. J. Dong, R. Y. Yang, R. P. Zou, and A. B. Yu, *Phys. Rev. Lett.* **96**, 145505 (2006).
- [39] M. Jerkins, M. Schroter, and H. L. Swinney, *Phys. Rev. Lett.* **101**, 018301 (2008).
- [40] D. R. S. Talbot and J. R. Willis, *IMA J. Appl. Math.* **35**, 39 (1985).
- [41] S. Torquato, *Annu. Rev. Mater. Res.* **32**, 77 (2002).
- [42] M. J. Beran, *Statistical Continuum Theories* (Interscience, New York, 1968).
- [43] P. Smith and S. Torquato, *J. Comput. Phys.* **76**, 176 (1988).
- [44] I. Taguchi, M. Kirashige, and K. Imai, *JSME Int. J., Ser. A* **49**, 265 (2006).
- [45] B. C. Collins, M.S. thesis, University of Illinois at Urbana-Champaign, 2008.
- [46] Z. Michalewicz, *Genetic Algorithms+Data Structures =Evolution programs* (Springer, Berlin, 1992).
- [47] J. L. Lions, *Some Methods in the Mathematical Analysis of Systems and their Control* (Gordon and Breach, New York, 1981).
- [48] C. Liu, *Exp. Mech.* **45**, 238 (2005).
- [49] S. Swaminathan and S. Ghosh, *J. Compos. Mater.* **40**, 605 (2006).
- [50] L. Massa, T. L. Jackson, and J. Buckmaster, *J. Propul. Power* **21**, 914 (2005).